Article

Journal of the Brazilian Chemical Society

https://dx.doi.org/10.21577/0103-5053.20240018

*J. Braz. Chem. Soc.* **2024**, *35*, 11, e-20240018, 1-16


# A Potential Sustainable Urea-Releasing Device Produced by a Solid-State Reaction

*Michelly Cristina G. Pellá,*[a] *Andressa Renatta Simão,*[a] *Antônia Millena O. Lima,*[a] *Marcos Roberto Mauricio,*[a] *Guilherme M. Pereira,*[b] *Rafael da Silva*[a] *and Adley F. Rubira*[a]*

[a]*Departamento de Química, Universidade Estadual de Maringá, Av. Colombo, 5790, 87020-900 Maringá-PR, Brazil*

[b]*Departamento de Ciências, Universidade Estadual de Maringá, Av. Reitor Zeferino Vaz, 87360-000 Goioerê-PR, Brazil*

This work produced chemically activated sugarcane bagasse-based activated carbon (AC) for the controlled release of urea. Fourier transform infrared (FTIR) and Raman analysis confirmed the presence of graphitic structures and multiple oxygen-containing functional groups. After the solid-state reaction that formed the material, their surface area reached 1401 $m^2 g^{-1}$ for the sample prepared with a pyrolysis temperature of 400 °C, a concentration of sodium hydroxide equivalent to 11 mol $L^{-1}$, and an activation temperature of 900 °C (AC 400-11-900). Zeta potential measures indicated negative charges at pH > 4, reaching almost (−50 mV) at pH 9. The adsorptive capacity of the AC with the highest surface area was equal to (758.7 ± 263.8) mg $g^{-1}$. Nevertheless, the matrix did not release the urea molecules previously adsorbed into it, which is appealing for fertilizer-releasing purposes because the activated carbon would be able to re-adsorb the non-absorbed urea molecules, sustaining nutrient availability for longer periods.

**Keywords:** agricultural application, biomass waste, statistical approach, design of experiments, urea

## Introduction

Aiming at "closing loops", circular economy involves reusing or repurposing goods that no longer suit their original goal or that have already fulfilled their goal.[1] It prevents the accumulation of resources that could be useful elsewhere. Plastic waste,[2] sewage sludge,[3,4] and biomass residues like olive stones,[5] corn-cob,[6] coconut shell,[7] peanut shell,[8] orange peel,[9] and sugarcane bagasse[10] are examples of wastes that could be converted into useful materials through the concept of the circular economy. Some of these biomass residues, like the sugarcane bagasse one, have been pyrolyzed after fulfilling their primary goal to produce energy and/or charcoals that could be later transformed into activated carbons, becoming a material with added value.

Defined as a carbonaceous material with porosity enclosed in it,[11,12] activated carbons are adsorptive particles widely used for the purification of water and air.[11] The production of activated carbons starts with the pyrolysis of the respective residue. It eliminates gas molecules from the structure of the precursor, forming charcoals.[11] The high surface areas that characterize activated carbons are achieved after physical or chemical activation steps.[13]

Physical activation involves the use of gas molecules (usually carbon dioxide and steam) and high temperatures to remove smaller molecules from the precursors, ultimately forming "holes" (or pores) in the charcoal structure.[14] Despite the efficiency observed in physical activation processes, chemical activation is still preferred because it tends to form particles of even higher surface areas.[13,14] In chemical activation processes, charcoal is impregnated with acid or base.[15] These ions (protons ($H^+$), or hydroxide ($^-OH$)) initially attack the functional groups that remain on charcoal after the pyrolysis, often converting them into simpler molecules, and the subsequent heating also leads to the elimination of these simpler molecules.[16] Literature reports indicate the successful production of materials with surface areas superior to 3200 $m^2 g^{-1}$.[17]

The unique characteristics of activated carbons, particularly their high surface area, led to a growing interest in other fields like energy storage systems,[18,19] the removal of contaminants from aqueous mediums,[20,21] and fertilizer-releasing devices,[22,23] for example. Their use as fertilizer-

*e-mail: michellepella57@gmail.com; afrubira@gmail.com
Editor handled this article: Célia M. Ronconi (Associate)

releasing devices is relatively new[24] and still has a lot to be explored in terms of release mechanisms, efficiency, suitability, and so on. Moreover, besides high surface areas, activated carbons still have polar functional groups (mostly nitrogen and oxygen-containing groups) in their structure,[25] favoring the formation of physical interactions with polar molecules like urea, for instance.

The production of activated carbons involves a solid-state reaction, as the molecular rearrangements that form their porous structure are the result of high temperatures.[26] Under natural conditions, the reactions required to form such pores would not be easily achieved, and would potentially be reversible. However, under the forced conditions employed in solid-state reactions, the rearrangements become permanent.

Therefore, given the structural features of activated carbons mentioned above, this work had two main goals: (*i*) evaluating the *in vitro* performance and efficiency of a sugarcane bagasse-based activated carbon, produced using solid-state reactions, as a urea release device; and (*ii*) determining the statistical effect of experimental conditions (pyrolysis temperature, base (KOH) concentration, and activation temperature) on the properties of the produced activated carbon samples.

The choice of applying an activated carbon as a urea-releasing device comes from the common use of biochar as a soil amendment or conditioner[27,28] to improve nutrient retention in the soil.[29,30] Besides, it represents a cleaner and potentially more sustainable alternative to fertilize the soil, besides fitting the appealing concept of the circular economy. It also represents another alternative to repurposing sugarcane bagasse waste.

## Experimental

### Materials

The sugarcane bagasse used in this work was gently donated by a local farmer from Maringá, Paraná, Brazil. Sodium chloride (NaCl), sodium hydroxide (NaOH), potassium hydroxide (KOH), and *para*-dimethylaminobenzaldehyde (*p*-DMAB; 99%) were acquired from Sigma-Aldrich (Burlington, USA). Hydrochloric acid (HCl; 37%) and urea (99%) were acquired from Synth (Diadema, Brazil). All reactants were used as received.

### Methods

#### Preparation of the activated carbon (AC)

The AC presented in this work was prepared from sugarcane bagasse. The bagasse was dried and ground before being immersed in a saturated solution of sodium dodecyl sulfate. The mixture was stirred for 24 h at 25 °C. After this time, the bagasse was filtrated and dried in a convection oven at 50 °C for 24 h.[31]

The activated carbon was prepared according to the methodologies described by Zhang *et al.*[32] and Abdul Rahman and co-workers,[33] with some modifications. Initially, the sugarcane bagasse was dried in an oven (T = 100 °C) for 24 h before the pyrolysis temperature. Known amounts of sugarcane bagasse were placed into clay supports and pyrolyzed in a tubular oven for 2 h under a nitrogen atmosphere (flow rate of 30 mL $min^{-1}$) at a heating rate of 10 °C $min^{-1}$. The sample was kept under the nitrogen atmosphere until reaching room temperature (T ca. 25 °C).

The pyrolyzed samples were placed in plastic beakers containing an excess of concentrated KOH solutions. The dispersions were magnetically stirred for 24 h under room temperature (T ca. 25 °C). Subsequently, the samples were vacuum-filtered to separate the solid material from the solution.

For the activation step, the samples were once again transferred into the clay supports and activated in the tubular oven for 3 h under a nitrogen atmosphere (flow rate of 30 mL $min^{-1}$) at a heating rate of 10 °C $min^{-1}$. The sample was kept under the nitrogen atmosphere until reaching room temperature (T ca. 25 °C).

The activated carbon samples (AC) were washed in distilled water until reaching pH 7. A solution of 0.1 M HCl was used to adjust the pH. The washed samples were separated from the solution by vacuum filtration, dried in an oven (T = 100 °C) for 24 h, and stored in a desiccator containing silica gel.

The experiment was structured using a $2^3$ experimental design with three central points. Table 1 displays the pyrolysis temperature, the KOH concentration, and the activation temperature (°C) used to prepare the AC samples. They were named AC X-Y-Z, in which AC means activated

**Table 1.** The pyrolysis temperature, KOH concentration, and activation temperature employed in the $2^3$ experimental design with 3 central points used to produce the AC X-Y-Z[a] samples

| Level | Pyrolysis temperature / °C | [KOH] / (mol $L^{-1}$) | Activation temperature / °C |
|---|---|---|---|
| Lowest (−1) | 400 | 7 | 600 |
| Central point (0) | 500 | 9 | 750 |
| Highest (+1) | 600 | 11 | 900 |

[a]AC X-Y-Z: AC means activated carbon, X refers to the pyrolysis temperature (T = 400, 500, or 600 °C), Y refers to the KOH concentration ([KOH] = 7, 9, or 11 mol $L^{-1}$), and Z refers to the activation temperature (T = 600, 750, or 900 °C). The samples from the central point also have the letters a, b, or c in their name merely to differentiate them.

carbon, X refers to the pyrolysis temperature (T = 400, 500, or 600 °C), Y refers to the KOH concentration ([KOH] = 7, 9, or 11 mol $L^{-1}$), and Z refers to the activation temperature (T = 600, 750, or 900 °C). The samples from the central point also have the letters a, b, or c in their name merely to differentiate them.

### Characterization

#### Fourier transform infrared spectroscopy (FTIR)

The FTIR analysis was performed using KBr pellets. Qualitative amounts of the AC samples were ground with 10 mg of KBr until producing a fine powder. The pellets were analyzed in a Thermo Scientific Nicolet iZ10 (Waltham, USA), from 4000 to 400 $cm^{-1}$. Each spectrum is the result of 128 scans at a resolution of 4 $cm^{-1}$.

The produced data was processed (baseline subtraction and data normalization) using data processing software.

#### X-ray diffraction (XRD)

The XRD patterns were acquired using a diffractometer from Shimadzu (Shimadzu 6000; Kyoto, Japan). The analysis was performed using monochromatic radiation (Cu Kα; λ = 1.5 Å), a current intensity of 30 mV, a voltage of 40 kV, and diffraction angles (2θ; degrees) ranging from 5 to 60°, acquired at a scanning rate of 2° $min^{-1}$.

The obtained data were processed (smoothing, baseline subtraction, and normalization) using data processing software. The percentage of crystallinity (Xc; %) was determined from the processed data using equation 1, in which Ap refers to the area of the peak, and At, the total area of the diffractogram (crystalline + amorphous regions).[10] The mathematical areas were determined by integration using end-points straight line as the baseline.

$$Xc\,(\%) = \frac{A_p}{A_t} \times 100 \quad (1)$$

The interlayer spacing of aromatic layers ($d_{002}$; nm) was calculated using equation 2, in which λ is the X-ray wavelength (λ = 0.1 nm).[34]

$$d_{002} = \frac{\lambda}{2\sin\theta_{002}} \quad (2)$$

The crystallite height ($L_c$; nm) was determined using equation 3, in which λ is the X-ray wavelength (λ = 0.1 nm), $k_c$ is a constant ($k_c$ = 0.9),[34-36] and $\beta_{002}$ and $\theta_{002}$ are, respectively, the full width at half maximum and the center of the peak 002. This parameter specifies the thickness of the stacking structure of a sample.[37]

$$L_c = \frac{k_c\lambda}{\beta_{002}\cos\theta_{002}} \quad (3)$$

The crystallite diameter ($L_a$; nm) was determined using equation 4; $k_a$ is a constant ($k_a$ = 1.8),[34-36] and $\beta_{001}$ and $\theta_{001}$ are, respectively, the full width at half maximum and the center of the peak 001.

$$L_a = \frac{k_a\lambda}{\beta_{001}\cos\theta_{001}} \quad (4)$$

The average number of effective aromatic layer *per* carbon crystallite ($N_{ave}$) was calculated using equation 5.

$$N_{ave} = \frac{L_c}{d_{002}} + 1 \quad (5)$$

#### Micro-Raman

Qualitative amounts of the AC X-Y-Z samples were placed in microscope slides and analyzed in a Witec Alpha 300R Raman Confocal microscope (Abingdon, United Kingdom) equipped with a laser of 532 nm. The analysis was performed from 3000 to 500 $cm^{-1}$, using an integration time of 1.5 s and a magnification of 20×. Each spectrum is the result of 20 scans.

The obtained data were processed (data smoothing, normalization, baseline subtraction, and deconvolution) using data processing software. The deconvolution of the spectra was performed using the Lorentz approach. The area of the peaks (determined by integration) was used to calculate the relative intensity (R) according to equation 6.

$$R = \frac{I_D}{I_G} \quad (6)$$

where $I_D$: intensity of the disorder-induced band and $I_G$: intensity of the first-order graphite band.

#### Thermogravimetric analysis (TG/DTG)

The thermal stability of the ACs was evaluated using thermogravimetric analysis. The analysis was performed in a TGA-50 from Shimadzu (Kyoto, Japan). Known amounts of the samples (ca. 7 mg) were transferred into alumina crucibles and heated from 30 to 1000 °C at a heating rate of 10 °C $min^{-1}$ and under a nitrogen atmosphere (50 mL $min^{-1}$).

The DTG results were produced by deriving the TGA data using data processing software. The results are discussed in Supplementary Information (SI) section.

#### Scanning electron microscopy (SEM)

The AC samples were initially placed on carbon tape.

They were subsequently gold-metalized in a metallizer (BAL-TEC model SCD 050; t = 120 s; Los Angeles, USA) and analyzed in a Quanta 250 (Hillsboro, USA) operating at an acceleration voltage of 20 kV and a current intensity of 30 mA. The images were acquired at magnifications of 2000 and 5000×.

The best sample was also analyzed in high-resolution SEM equipment (Scios; Thermo Fisher Scientific; Waltham, USA). After metallization as described above, the sample was analyzed at a current intensity of 0.10 nA, at magnifications of 25000 and 120000×.

### Zeta potential

The zeta potential of the AC X-Y-Z samples was assessed by dispersing the samples in 5 mL of 0.01 M NaCl solution using an ultrasonic bath (5 min at 40 kHz; Odontobras Ultrasonic Cleaner 1440 D; São Paulo, Brazil). The zeta potential was evaluated in 4 different pH values (pH = 3, 5, 7, and 9; adjusted using 0.1 M solutions of NaOH and HCl) using a Malvern Zetasizer Nano ZSP (Malvern, United Kingdom).

### X-ray photoemission spectroscopy (XPS)

The XPS analysis was performed in Scienta Omicron ESCA+ (Uppsala, Sweden) equipment with a high-performance hemispheric analyzer (EAC2000) with an Al Kα source (1486.7 eV). The analysis was performed in an ultra-high vacuum ($10^{-9}$ Pa). The survey scans were collected from 0 to 1200 eV, and the high-resolution scans were acquired between 278 and 298 eV for C 1s, 522 and 542 eV for O 1s, and 392 and 412 for N 1s. The spectra were recorded at constant pass energy (20 eV) and 0.05 eV *per* step for the high-resolution spectra. Surface charging effects were excluded using a charge neutralizer (CN10). The obtained results were processed using Casa XPS.[38]

The degree of oxidation $D_{ox}$ was determined using equation 7, in which $\sum A_{O1s}$ refers to the sum of the area of the peaks from the O 1s spectra; $A_{C_{graphitic}}$ and $A_{\pi-\pi}$ are the area referent to the graphitic peaks from the C 1s spectra.[39]

$$D_{ox} = \frac{\sum A_{O1s}}{A_{C_{graphitic}} + A_{\pi-\pi}} \quad (7)$$

### $N_2$ sorption analysis

The AC X-Y-Z samples were degasified for 460 min at 300 °C (Degas FlowPrep 060 from Micromeritics; Norcross, USA). The $N_2$ sorption/desorption analysis was performed using a TriStar II Surface Area and Porosity (from Micromeritics; Norcross, USA), and the Brunauer-Emmett-Teller (BET) and Barrett-Joyner-Halenda (BJH) calculations were performed using the software provided by the manufacturer.

### Adsorption and release of complexed urea

The adsorption analysis was performed using urea complexed with *p*-DMAB due to the unreliability of detecting pure urea using UV-Vis spectrophotometry,[40] which is a method based on the absorption of radiation by a sample.[41] A *p*-DMAB stock solution was prepared by adding 4 g of *p*-DMAB and 4 mL of sulfuric acid into a volumetric flask and completing the volume to 100 mL using ethanol. The complexed urea stock solution was prepared by dissolving 0.7 g of urea and 43 mL of the *p*-DMAB solution into 500 mL of 0.1 M NaCl solution (final pH = 5).

The adsorption assay started by transferring ca. 1.3 mg of the AC sample with the highest surface area (AC 400-11-900) into a plastic flask containing 25 mL of the complexed urea stock solution. The absorbance of the solution was measured immediately after adding the AC sample, and this value was used for corrections. The flasks were sealed to prevent solvent evaporation. The analysis was performed in triplicate, and the samples were orbitally stirred (50 rpm; T = 25 °C) until reaching the adsorption equilibrium, characterized by a stable region in the graph (parallel to the x-axis).

The adsorption was assessed using a UV-Vis spectrophotometer from Thermo Fisher Scientific (Waltham, USA), model Genesys 10S UV-Vis. Aliquots were collected from the flasks, placed in a quartz cuvette (without previous treatment), and analyzed at 422 nm.[42] The aliquots were returned to the flasks after the measures. Pure 0.1 M NaCl was used as the blank for these experiments.

The adsorptive capacity ($q_t$; mg $g^{-1}$) was determined using equation 8. In this equation, $c_0$ and $c_t$ refer to the concentration at t = 0, and at time t, V is the volume of stock solution added to the tubes (V = 25 mL), and w is the weight of sample added into the flask. The concentration values were determined using a linear equation obtained from the calibration curve.

$$q_t = \frac{(c_0 - c_t)V}{w} \quad (8)$$

The release assay was performed after the samples reached the adsorption equilibrium. The supernatant was carefully removed using a Pasteur's pipette, and 25 mL of 0.1 M NaCl was subsequently added into the tubes. Once again, the absorption was measured immediately after this step, and the obtained value was used for corrections. The absorbance was measured as described for the adsorption assay.

The results from the release assay are expressed in terms of absorbance *versus* time due to the methodology used in this work. SI section presents further discussions regarding the structure of the methodology employed for the determination of the adsorption and release of complexed urea.

### Statistical analysis

Statistical analyses were performed by analysis of variance (ANOVA) and effects. The analyzes were performed in Statistica 10,[43] and Minitab 19.[44] Interaction plots were constructed whenever necessary. The tables of effect are all presented in the SI section.

## Results and Discussion

### Physical-chemical characterizations

### Chemical composition and yield

Table 2 presents the results of the elemental analysis of the AC X-Y-Z samples and the respective yield. The total yield was calculated using the mass of each sample obtained after the washing process post-activation. Therefore, the shown yield results already account the losses during each step, including the filtration processes.

As expected in pyrolysis-involving processes, the total yield, which is the percentage of sample mass obtained at the end of the synthetic route, is very low. It is the result of the loss of several smaller molecules formed as the temperature rises, forcing the occurrence of solid-state reactions that ultimately lead to chain rearrangements and gas evolution. Despite the loss of innumerable types of smaller molecules, the final material still presents elements other than carbon and hydrogen, as confirmed by the data from Table 2.

### FTIR

Functional groups present in the AC X-Y-Z samples were determined by FTIR analysis. Figures 1a, 1d and 1g depict the obtained results. The band centered at 3454 $cm^{-1}$ matches the stretching of hydroxyl (–OH) groups.[41] It suggests the presence of water molecules adsorbed onto the surface of the samples.[25] Nonetheless, it could also indicate the presence of –OH groups attached to carbon atoms.[10] The bands between 2965 and 2851 $cm^{-1}$ describe the stretching of –CH bonds.[41,45] The other two bands match the stretching of C–C $sp^2$ (1580 $cm^{-1}$) and C–O (1096 $cm^{-1}$) bonds,[41,46] respectively. The observance of a C–O band in the spectra reinforces the presence of hydroxyl groups (–C–OH),[10] but it could indicate the presence of esters, anhydrides, and carboxylic acids.[41]

Regardless of the experimental conditions, all samples presented the same bands in the same wavenumbers. The difference in intensity and band shape might be the result of the variable amount of AC in each pellet, which was a consequence of the different sizes presented by the AC samples (as confirmed by results not yet discussed). The non-homogeneity of sizes prevented the production of KBr pellets using the same mass of AC, changing the concentration of functional groups in the pellets. It consequently affected the intensity and definition of some of the bands.

### XRD

The structure of ACs resembles the structure of graphite; however, the irregular distance between the layers and the impossibility of converting the AC into an organized

**Table 2.** The elemental composition of the AC X-Y-Z[a] samples, and the respective yield of each sample

| Sample | C / % | H / % | O / % | N / % | Total yield / % |
|---|---|---|---|---|---|
| AC 400-7-600 | 76.8 ± 0.1 | 2.0 ± 0.0 | 20.9 ± 0.1 | 0.3 ± 0.0 | 15.1 |
| AC 400-7-900 | 64.0 ± 0.2 | 3.1 ± 0.1 | 32.9 ± 0.1 | 0.0 ± 0.0 | 11.5 |
| AC 400-11-600 | 78.7 ± 0.5 | 2.2 ± 0.0 | 18.9 ± 0.5 | 0.2 ± 0.0 | 16.1 |
| AC 400-11-900 | 62.3 ± 0.2 | 2.8 ± 0.0 | 34.9 ± 0.2 | 0.0 ± 0.0 | 12.6 |
| AC 600-7-600 | 80.3 ± 0.3 | 2.1 ± 0.0 | 17.1 ± 0.3 | 0.5 ± 0.0 | 16.5 |
| AC 600-11-600 | 80.8 ± 0.0 | 2.1 ± 0.1 | 16.7 ± 0.1 | 0.4 ± 0.0 | 17.9 |
| AC 600-7-900 | 71.8 ± 0.4 | 2.1 ± 0.0 | 25.9 ± 0.4 | 0.1 ± 0.1 | 15.6 |
| AC 600-11-900 | 70.9 ± 0.6 | 2.4 ± 0.0 | 26.5 ± 0.6 | 0.2 ± 0.0 | 15.1 |
| AC 500-9-750a | 70.3 ± 0.2 | 2.1 ± 0.1 | 27.1 ± 0.3 | 0.5± 0.0 | 14.7 |
| AC 500-9-750b | 64.5 ± 0.9 | 2.6 ± 0.4 | 32.3 ± 0.4 | 0.5 ± 0.1 | 29.7 |
| AC 500-9-750c | 56.3 ± 0.3 | 2.1 ± 0.2 | 41.1 ± 0.0 | 0.5 ± 0.1 | 26.2 |

[a]AC X-Y-Z: AC means activated carbon, X refers to the pyrolysis temperature (T = 400, 500, or 600 °C), Y refers to the KOH concentration ([KOH] = 7, 9, or 11 mol $L^{-1}$), and Z refers to the activation temperature (T = 600, 750, or 900 °C). The samples from the central point also have the letters a, b, or c in their name merely to differentiate them.

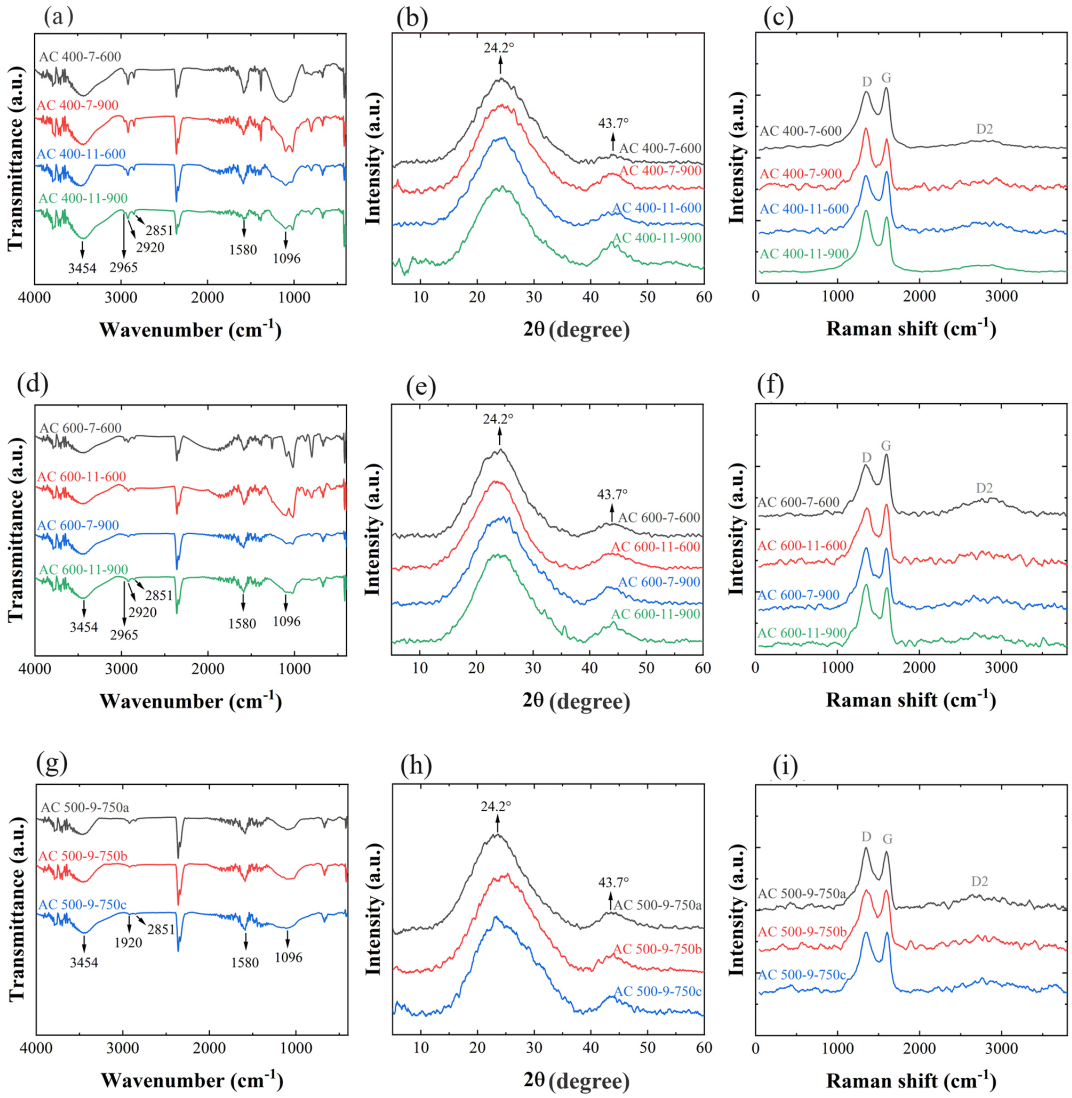


**Figure 1.** FTIR (KBr) (left), XRD (center), and Raman (left) spectra of the AC X-Y-Z samples, in which AC stands for activated carbon, X refers to the pyrolysis temperature (T = 400, 500, or 600 °C), Y refers to the KOH concentration ([KOH] = 7, 9, or 11 mol $L^{-1}$), and Z refers to the activation temperature (T = 600, 750, or 900 °C). The samples from the central point also have the letters a, b, or c in their name merely to differentiate them.

structure even by heating it at temperatures superior to 2000 °C (non-graphitizable) are the main differences between them.[12] The XRD analysis (Figures 1b, 1e, and 1h) confirmed the amorphous character of the AC samples produced in this work. They presented two broad peaks at 2θ ca. 24.2° and ca. 43.7°, matching the diffraction patterns 002 and 100,[46,47] respectively. The 002 peak describes the height of the aromatic layer formed by the polycondensation of aromatic nucleus, while the 100 peak determines the condensation degree of the aromatic rings.[34]

Lattice parameters were determined from the XRD data and a statistical analysis was performed to determine the effect of individual and correlated experimental parameters on the structure of the AC X-Y-Z samples. SI section presents the statistical data and the respective discussion.

### Raman

The Raman shift of the AC X-Y-Z samples was also evaluated. The graphs of Figures 1c, 1f, and 1i display the obtained results. All samples displayed three main bands. The first band, observed at ca. 1350 $cm^{-1}$, is called the D-band. It originates from the vibration of $sp^3$-hybridyzed carbon atoms on the edge of the aromatic layer.[48,49] These $sp^3$-hybridyzed carbon atoms create a disordered amorphous structure that ultimately leads to defects in the structure of the activated carbon.[49,50] It justifies the name of the band: disorder-induced band (D).[51]

The second band observed in the spectra (ca. 1586 $cm^{-1}$; G-band) is the result of the in-plane stretching of all of the $sp^2$-hybridyzed carbon atoms.[50,51] This band is the result of the vibration of the perfectly ordered graphite (G) layer (G-band).[51] The third band observed in the

spectra (ca. 2804 $cm^{-1}$) describes a second-order band of the D-band (2D).[51] The intensity of this band depends on the ordering of the graphitic layer,[52] and the packing of the three-dimensional structure affects the intensity of this band.[53] In this case, the bigger the disorder or the smaller the crystal size, the weaker and broader this band becomes.[54]

The deconvoluted spectra (Figure S2, SI section) also highlight two other bands. These bands, centered at ca. 1174 and ca. 1564 $cm^{-1}$, appear when the material has random structures in it.[55] The relative intensity is used to determine the degree of organization of the activated carbon.[56,57]

Table 3 presents the center position of each band observed in the Raman spectra and the relative intensity, determined from the $I_D/I_G$ ratio.

The literature reports that the lower the R, the higher the organization of the material.[53,58] The R values from this work ranged from 1.7 (AC 600-7-900) to 4.5 (AC 500-9-750c). According to the literature,[59] graphite has an R intensity close to 0.14 (at $\lambda$ = 532 nm). Therefore, although the AC samples produced in this work achieved a certain level of organization (as confirmed by the G-band), they were far from having perfectly crystalline graphitic structures. It agrees with the XRD results.

Statistical analysis (Figure S1g, SI section) indicated that higher pyrolysis and activation temperatures (1by3) decreased R by 1.2. This decrease is the reflection of the transversal condensation of aromatic rings.

## XPS

The XPS technique was also used to determine the functional groups present in the AC samples.[39] This analysis was only performed for AC 400-11-900. This sample presented the highest surface area ("$N_2$ sorption/desorption" sub-section) and was, therefore, further characterized. Figure 2 presents the obtained results regarding the survey scanning and the high-resolution spectra.

The asymmetrical C 1s spectra[60] presented peaks characteristic of graphitic carbon atoms (284.0 eV), π-π transitions (290.8 eV), and C–O bonds (phenol, alcohol, and ether; 284.55 eV),[39] agreeing with the FTIR and Raman results. However, while the noise observed at the FTIR carbonyl range (1750-1640 $cm^{-1}$) prevented their identification, XPS spectra clearly indicated their presence on the surface of AC 400-11-900. Two carbonyl peaks appeared at 286.0 and 288.6 eV, describing, respectively, C=O, and COO bonds from esters and carboxylates.[39,61] Regarding the oxygen signal, the deconvolution indicated the presence of negatively charged oxygen species (probably hydroxide anions, $^{-}OH$)[62] as well as carbonyl and C–O bonds.

The percentage of the area (Table 4) agrees with the Raman results, confirming that the graphitic portion of AC 400-11-900 was still smaller than the disordered portion. Furthermore, the degree of oxidation was equal to 0.4. The presence of oxygen-containing groups increases the probability of hydrogen-bonding formation with adjacent molecules.

The results obtained from these characterization techniques suggested the successful formation of activation carbons with oxygen-containing groups on their surface. Furthermore, these techniques also indicated that the solid-state reactions that took place during the production of the ACs led to the formation of a material simultaneously containing more and less organized regions, with potential suitability for adsorptive and desorptive purposes.

**Table 3.** The center position of the bands observed in the Raman shift, the correlation coefficient ($R^2$), and the relative intensity (R) of the AC X-Y-Z[a] samples

| Sample | Band / $cm^{-1}$ | | | | | $R^2$ | $R^2_{I_D/I_G}$ |
|---|---|---|---|---|---|---|---|
| | $R_1$ | D | $R_2$ | G | 2D | | |
| AC 400-7-600 | 1139.0 | 1350.0 | – | 1593.0 | 2798.0 | 1.0 | 2.2 |
| AC 400-7-900 | 1210.0 | 1335.0 | 1530.0 | 1593.0 | 2821.0 | 1.0 | 2.8 |
| AC 400-11-600 | 1178.0 | 1358.0 | – | 1593.0 | 2790.0 | 1.0 | 2.3 |
| AC 400-11-900 | 1123.0 | 1350.0 | 1523.0 | 1593.0 | 2790.0 | 1.0 | 2.3 |
| AC 600-7-600 | 1139.0 | 1350.0 | 1608.0 | 1577.0 | 2838.0 | 1.0 | 3.9 |
| AC 600-11-600 | 1225.0 | 1358.0 | 1616.0 | 1585.0 | 2806.0 | 1.0 | 3.2 |
| AC 600-7-900 | 1249.0 | 1350.0 | 1491.0 | 1593.0 | 2838.0 | 1.0 | 1.7 |
| AC 600-11-900 | 1186.0 | 1342.0 | 1484.0 | 1601.0 | 2759.0 | 1.0 | 2.0 |
| AC 500-9-750a | 1154.0 | 1350.0 | 1616.0 | 1569.0 | 2751.0 | 1.0 | 3.8 |
| AC 500-9-750b | 1186.0 | 1358.0 | 1608.0 | 1569.0 | 2806.0 | 1.0 | 3.8 |
| AC 500-9-750c | 1123.0 | 1358.0 | 1608.0 | 1577.0 | 2853.0 | 1.0 | 4.5 |

[a]AC means activated carbon, X refers to the pyrolysis temperature (T = 400, 500, or 600 °C), Y refers to the KOH concentration ([KOH] = 7, 9, or 11 mol $L^{-1}$), and Z refers to the activation temperature (T = 600, 750, or 900 °C). The samples from the central point also have the letters a, b, or c in their name merely to differentiate them.

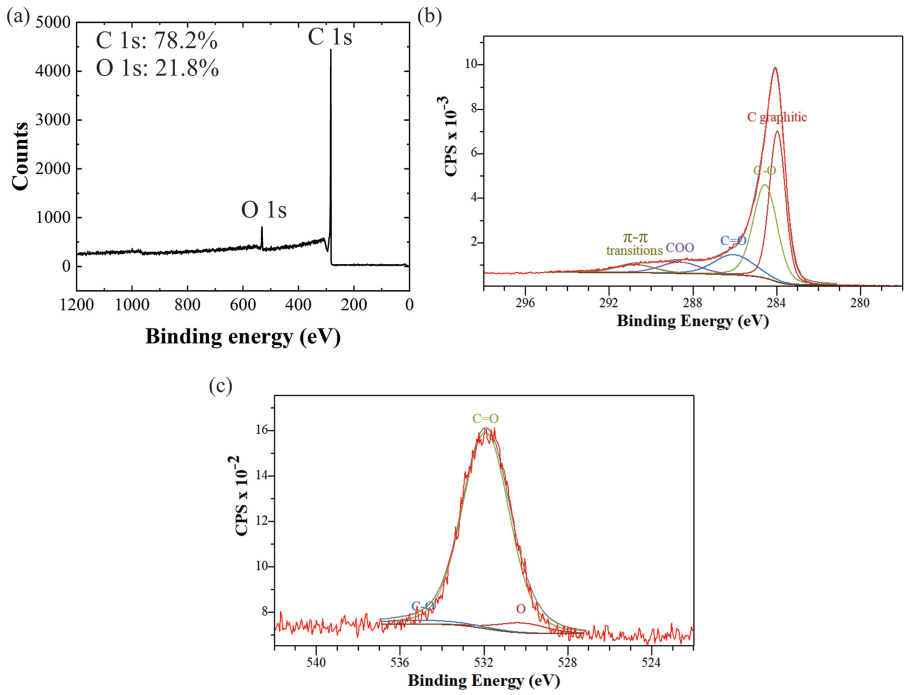


**Figure 2.** XPS results of the (a) survey scanning, and the high-resolution scanning of (b) C 1s, and (c) O 1s.

**Table 4.** XPS signal, peak attribution, center peak position, full width at half maximum (FWHM), area, and percentage of area (Area) of AC 400-11-900

| Signal | Peak | Position / eV | FWHM / eV | Area / eV | Area / % |
|---|---|---|---|---|---|
| C 1s | C graphitic | 283.98 | 0.90 | 7000.67 | 38.63 |
| | C–O | 284.55 | 1.35 | 6539.29 | 36.08 |
| | C=O | 286.05 | 2.25 | 2343.60 | 12.93 |
| | COO | 288.61 | 2.25 | 1312.72 | 7.24 |
| | π-π transitions | 290.77 | 2.25 | 927.95 | 5.12 |
| O 1s | O | 530.21 | 2.7 | 134.88 | 4.69 |
| | C=O | 531.91 | 2.65 | 2638.79 | 91.81 |
| | C–O | 534.91 | 5.35 | 100.39 | 3.49 |

## Morphology

The morphology of AC 400-11-900 was evaluated using SEM. Figure 3 presents the results of the SEM analysis of sugarcane bagasse and AC 400-11-900 and high-resolution SEM micrographs of AC 400-11-900. Sugarcane bagasse (SCB; Figure 3a) had a smooth, non-porous, and irregular surface. The particular irregularities observed on the edges of SCB are the result of the washing and milling used to reduce the size of SCB.[63]

The activated carbon sample (AC 400-11-900) also presented irregularly-shaped pieces (Figure 3b). However, their surface had different characteristics. Some of the pieces were entirely porous, while others had only a few visible pores. This porosity difference becomes more evident in the high-resolution micrographs (Figure 3c). The removal of the activating agent (KOH) during the activation step[64] and the different distribution of atoms throughout the aromatic layer justify this behavior.[65]

The non-observance of lattice fringes in Figure 3c reinforces the predominantly amorphous characteristic of AC 400-11-900, agreeing with the XRD and Raman results. Furthermore, the high porosity of AC 400-11-900, as confirmed in Figure 3c, justifies the high surface area of this sample.

The morphology of the activated carbon prepared in this work was similar to the one reported by El Naga *et al.*[64] They used zinc chloride ($ZnCl_2$) to activate SCB. The SEM results suggested the formation of interconnected porous structures with randomly shaped and distributed pores.

## Surface properties

### Zeta potential

Zeta potential analysis were performed to determine the charge on the surface of the AC X-Y-Z samples. Table 5 presents the zeta potential values of each sample

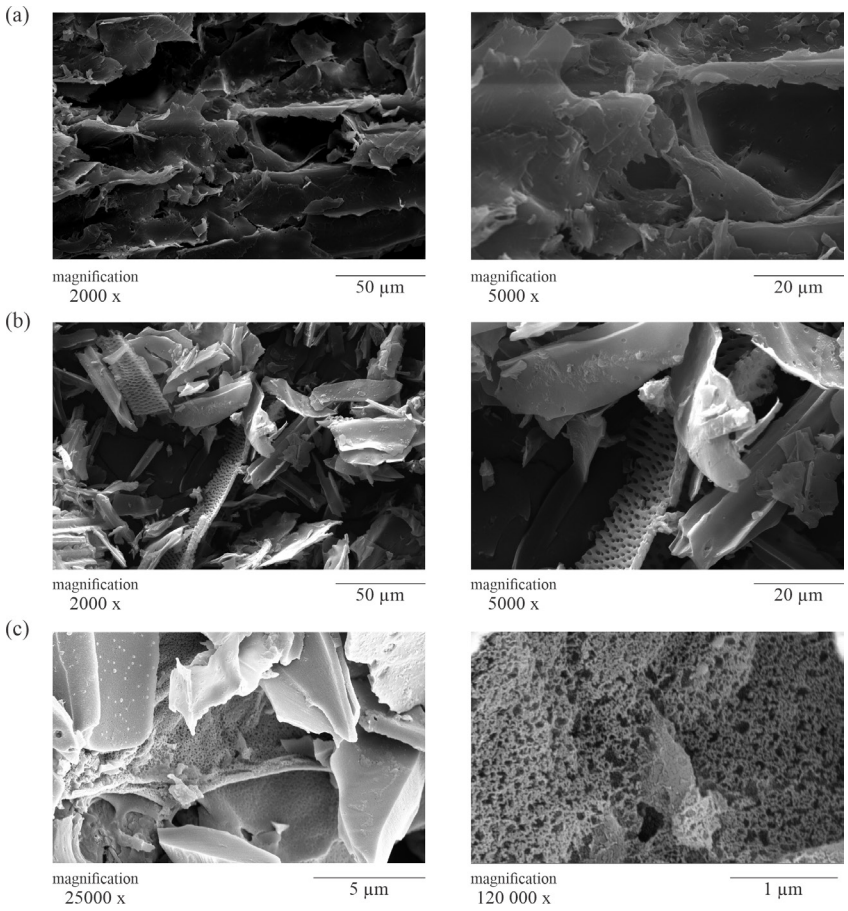


**Figure 3.** SEM micrographs of (a) sugarcane bagasse, and (b) AC 400-11-900; (c) high-resolution SEM micrograph of AC 400-11-900.

as a function of the pH, ranging from pH 3 to pH 9, and Figure S5 (SI section) provides a visual comparison of the results. The zeta potential of the samples ranged from (+25.8 ± 0.7) mV (AC 600-7-900; pH 3) to (–54.6 ± 1.8) mV (AC 400-11-600; pH 9), confirming the presence of charged groups on the material.

The results evidenced an intriguing tendency: all samples produced at the highest activation temperature (T = 900 °C;) displayed positive charges on their surface at pHs < 4. The change from positive to negative charges suggests the existence of a point of zero charge ($pH_{pzc}$) on the samples. In the point of zero charge, the amount of negative charge counterbalances the amount of positive charge, leading to a null net charge (0 mV).[65] It suggests the presence of polar groups that can subtract protons from the medium. In this case, pH > $pH_{pcz}$ leads to negatively charged particles, while pH < $pH_{pzc}$, to positively charged particles.[66-68]

The previous results suggested that higher activation temperatures increased the surface area of the samples due to the loss of gas molecules like CO and $CO_2$ ("Physical-chemical characterizations" sub-section). It, therefore, decreased the number of polar groups capable of subtracting protons from the medium. The positive charge observed on samples AC 400-7-900, AC 400-11-900, AC 600-7-900, and AC 600-11-900 suggests that the amount of $H^+$ species in the medium exceeded the number of polar groups, being able to protonate them to reach the positive charge. It also suggests an excess of polar groups in the samples produced using the activation temperature of 600 °C. In this case, even though the $H^+$ species from the acid mediums successfully protonated some of the polar groups (as confirmed by the decrease in the zeta potential value), not all the groups were protonated, preserving a negative net charge on the particles.

The sample AC 500-9-750a was an exception in all the performed analyses, especially considering it was produced using the same conditions used for samples AC 500-9-750b and AC 500-9-750c. The observed differences might be the result of (*i*) different cellulose/lignin ratios, (*ii*) different sizes of sugarcane bagasse particles used for the production of the samples, or (*iii*) the combination of (*i*) and (*ii*).

The same reasons might explain the unexpected results observed for sample AC 400-11-900. Since it was the sample with the highest surface area among all samples (Table 6), its zeta potential value should have

**Table 5.** The zeta potential values of the AC X-Y-Z[a] samples as a function of the pH

| Sample | Zeta potential / mV | | | |
|---|---|---|---|---|
| pH | 3.3 | 5.4 | 7.5 | 9.3 |
| AC 400-7-600 | –21.60 ± 1.61 | –43.90 ± 2.55 | –42.20 ± 4.39 | –50.30 ± 3.82 |
| AC 400-7-900 | 8.51± 0.96 | –10.50 ±1.13 | –30.50 ± 0.14 | –44.00 ± 0.21 |
| AC 400-11-600 | –9.90 ± 0.51 | –39.50 ±0.01 | –42.30 ± 1.66 | –54.60 ±1.76 |
| AC 400-11-900 | 5.74 ±1.50 | –21.60 ± 0.28 | –23.40 ± 7.07 | –36.60 ± 0.42 |
| AC 600-7-600 | –5.24 ± 1.38 | –23.20 ± 1.13 | –35.30 ± 0.92 | –47.00 ±1.48 |
| AC 600-11-600 | –27.6 ± 0.67 | –29.50 ± 2.33 | –36.70 ± 0.28 | –44.80 ± 0.85 |
| AC 600-7-900 | 25.80 ± 0.74 | –15.90 ± 1.91 | –33.40 ± 2.12 | –44.50 ± 1.23 |
| AC 600-11-900 | 13.10 ± 1.06 | –21.30 ± 1.97 | –29.80 ± 2.00 | –37.00 ± 4.24 |
| AC 500-9-750a | 11.4 ± 3.73 | 6.61 ± 0.22 | –24.30 ± 2.71 | –31.80 ± 1.77 |
| AC 500-9-750b | –2.42 ± 0.04 | –23.30 ± 1.38 | –34.40 ± 1.62 | –41.00 ± 0.68 |
| AC 500-9-750c | –3.12 ± 1.05 | –20.80 ± 0.14 | –33.30 ± 1.63 | –41.70 ± 2.95 |

[a]AC means activated carbon, X refers to the pyrolysis temperature (T = 400, 500, or 600 °C), Y refers to the KOH concentration ([KOH] = 7, 9, or 11 mol $L^{-1}$), and Z refers to the activation temperature (T = 600, 750, or 900 °C). The samples from the central point also have the letters a, b, or c in their name merely to differentiate them.

been the highest. However, it ranged from (+5.7 ± 1.5) to (–36.6 ± 0.4) mV. On the other hand, the loss of neutral gas molecules (small hydrocarbons, for example) might justify the high surface area presented by this sample.

The zeta potential values observed in this work were similar to the ones reported by Gonçalves *et al.*[69] The zeta potential of their sugarcane bagasse-based activated carbon was (–46.6 ± 0.8) mV, measured in $H_2O$ Milli-Q.

### $N_2$ sorption/desorption

The adsorptive capacity of the AC X-Y-Z samples was evaluated according to the models of Langmuir and Brunauer, Emmett, and Teller (BET). Langmuir's model describes monolayer adsorption. This model assumes that the adsorption cannot occur in more than one layer, that all the adsorption sites are equivalent, and that the capacity of adsorbing a molecule onto the surface of a site does not depend on the occupation of adjacent adsorption sites.[70] The BET model describes adsorptions in which the molecules directly adsorbed onto the surface act as a substrate, allowing the formation of a new layer. The new layer can adsorb new molecules, and the formation of new layers continues infinitely.[71] Nevertheless, the BET theory only explains the linear adsorption behavior usually observed at $P/P_0$ up to 0.3.[72]

Figure 4 shows the $N_2$ sorption (gray) and desorption (red) isotherms presented by the AC X-Y-Z samples. All isotherms described the type-II adsorption profiles[71] characteristic of activated carbon.[73] Type-II adsorption characterizes multilayer adsorption. It allows the uptake of molecules even at relative pressures ($P/P_0$) close to 1,[74,75] and it is well-described by the BET equation.[74,76] This type of reversible adsorption usually appears in macro[74] and microporous materials.[77]

Hysteresis loops appeared for all samples but AC 400-7-600 during the desorption of $N_2$ (red circles; Figure 4). These loops are the result of a metastable multilayer caused by the condensation of gas molecules[78] inside capillaries present in the mesoporous structure of the adsorbent.[77,79] In this case, the subsequent desorption of the gas molecules from the pores depends more on the degree of blocking of the channels from the pore to the surface than on shape-related parameters.[80]

For nitrogen, at T = 77 K, the hysteresis loop has a cut-off at $P/P_0$ between 0.5 and 0.4.[81,82] It usually appears in materials whose pores have diameters between 2 and 50 nm.[83] The diameter of pores from the normal distribution plots from Figure 4 supports this statement. Even though the AC X-Y-Z samples presented a wide mesopore diameter distribution, the most observed diameter was close to 50 nm, as shown in Table 6.

Although the obtained isotherms match the type-II adsorption, which usually leads to an H3-shaped hysteresis loop,[77] the elongation along the relative pressure axis (x-axis) closing at a critical $P/P_0$ value characterizes the H4 shape.[84] It happens when the adsorbed molecules undergo blockage in the pores.[85] However, this hysteresis shape is common in activated carbons.[77]

The samples AC 400-11-600 AC 600-7-600, and AC 600-11-600 also presented low-pressure hysteresis ($P/P_0 < 0.4$).[86] It happens when the structure of non-rigid pores deforms, preventing the desorption of the gas molecules or when chemical adsorption occurs instead of physical adsorption.[79] The deformation of the non-rigid

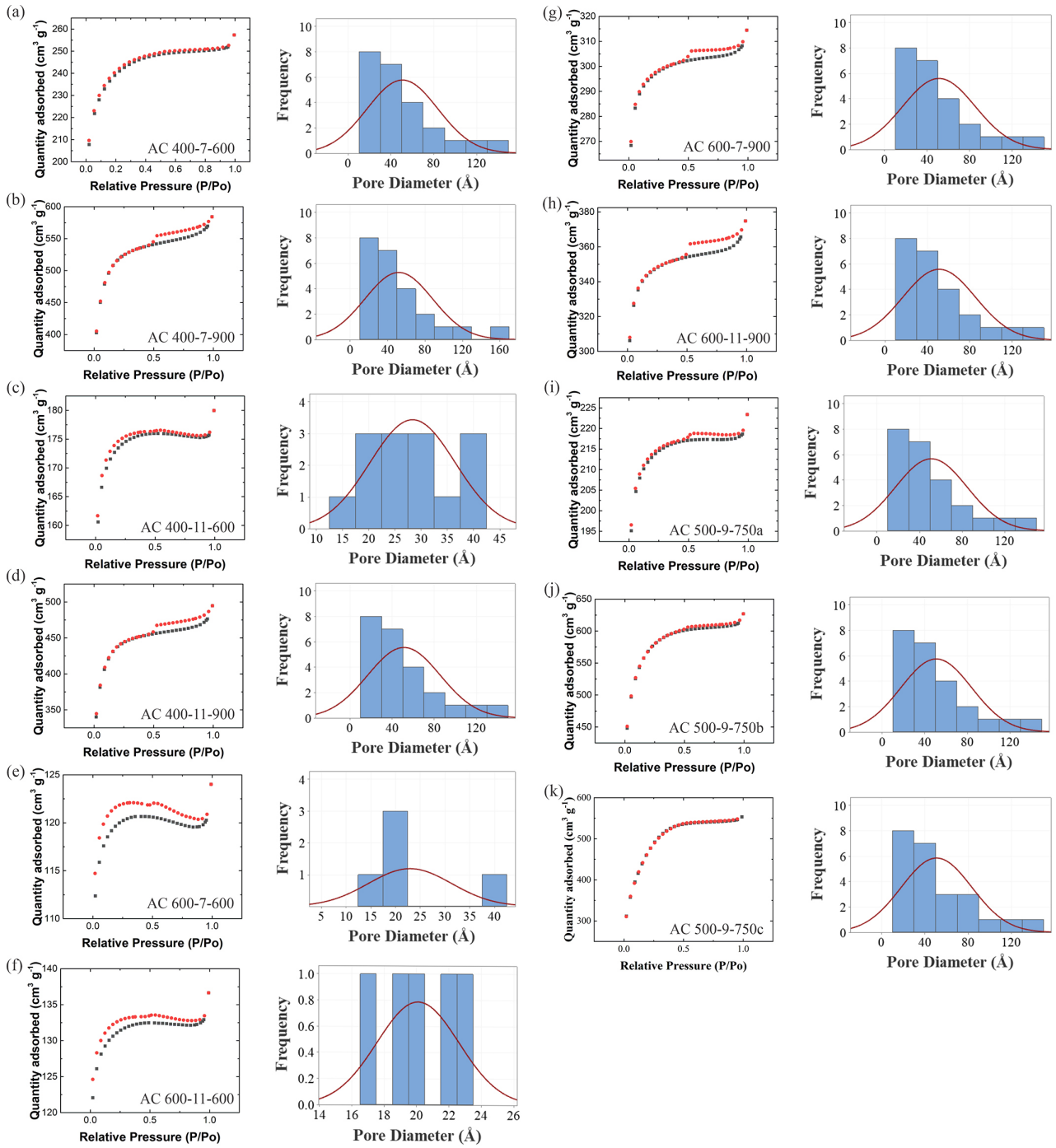


**Figure 4.** Isotherm linear plot of the $N_2$ sorption (gray) and desorption (red) (left) and normal distribution of the diameters of the mesopores (Å) (right) of the samples (a) AC 400-7-600, (b) AC 400-7-900, (c) AC 400-11-600, (d) AC 400-11-900, (e) AC 600-7-600, (f) AC 600-11-600, (g) AC 600-7-900, (h) AC 600-11-900, (i) AC 500-9-750a, (j) AC 500-9-750b, and (k) AC 500-9-750c. AC means activated carbon, *X* refers to the pyrolysis temperature (T = 400, 500, or 600 °C), *Y* refers to the KOH concentration ([KOH] = 7, 9, or 11 mol $L^{-1}$), and *Z* refers to the activation temperature (T = 600, 750, or 900 °C). The samples from the central point also have the letters a, b, or c in their name merely to differentiate them.

pores occurs when the adsorbed molecule swells in the pore. It consequently increases the size of the molecule and requires more extreme conditions (higher temperatures, for example) to desorb the molecule.[84] The aforementioned samples were the ones with the smallest mesopore diameter among all samples (ca. 20 nm).

As mentioned, the obtained sorption/desorption curves (Figure 4) were assessed using the models of BET and Langmuir. Even though both models presented high correlation coefficient ($R^2$), values (differing from the third significant digit on) for the surface area, the BET model is still the model that best fits the experimental data because

**Table 6.** The surface area determined according to the BET model, the area and the volume of micropores, and the pore diameter of the AC X-Y-Z[a] samples

| Sample | Surface area / ($m^2$ $g^{-1}$) | $R^2$ | Area of micropores / ($m^2$ $g^{-1}$) | Volume of micropores / ($cm^3$ $g^{-1}$) | $R^2$ | Diameter of mesopore / Å |
|---|---|---|---|---|---|---|
| AC 400-7-600 | 761.8 | 1.0 | 582.9 | 0.3 | 1.0 | 50.7 ± 33.2 |
| AC 400-7-900 | 1118.4 | 1.0 | 769.2 | 0.4 | 1.0 | 51.9 ± 36.3 |
| AC 400-11-600 | 546.0 | 1.0 | 488.2 | 0.2 | 1.0 | 28.4 ± 8.1 |
| AC 400-11-900 | 1401.5 | 1.0 | 960.9 | 0.5 | 1.0 | 51.2 ± 34.4 |
| AC 600-7-600 | 375.4 | 1.0 | 343.2 | 0.2 | 1.0 | 23.0 ± 8.4 |
| AC 600-11-600 | 410.8 | 1.0 | 369.6 | 0.2 | 1.0 | 20.1 ± 2.5 |
| AC 600-7-900 | 933.4 | 1.0 | 819.9 | 0.4 | 1.0 | 51.1 ± 34.2 |
| AC 600-11-900 | 1092.9 | 1.0 | 935.1 | 0.5 | 1.0 | 51.1 ± 34.3 |
| AC 500-9-750a | 1035.9 | 1.0 | 852.5 | 0.2 | 1.0 | 50.9 ± 33.8 |
| AC 500-9-750b | 1829.9 | 1.0 | 1162.0 | 0.58 | 1.0 | 50.8 ± 33.3 |
| AC 500-9-750c | 2285.2 | 1.0 | 394.5 | 0.18 | 1.0 | 51.8 ± 34.5 |

[a]AC -X-Y-Z: AC means activated carbon, X refers to the pyrolysis temperature (T = 400, 500, or 600 °C), Y refers to the KOH concentration ([KOH] = 7, 9, or 11 mol $L^{-1}$), and Z refers to the activation temperature (T = 600, 750, or 900 °C). The samples from the central point also have the letters a, b, or c in their name merely to differentiate them. $R^2$: correlation coefficient.

the obtained isotherms are characteristic of a multilayer adsorption. Table 6 presents the values for the surface area determined using the BET model, area and volume of micropores, and resumes the pore diameters.

The experimental conditions led to considerably high surface areas, ranging from 375.4 to 1401.5 $m^2$ $g^{-1}$ for samples AC 600-7-600 and AC 400-11-900, respectively. These same samples presented an area of micropores ranging from 343.2 to 960.9 $m^2$ $g^{-1}$ and pore volumes ranging from 0.17 to 0.48 $cm^3$ $g^{-1}$. Although the central point samples (AC 500-9-750a, b, and c) were a triplicate of the same condition, they presented a wide variation in the surface area value, ranging from 1035.9 to 2285.2 $m^2$ $g^{-1}$. This variation might be a result of samples with different sizes after the ball milling of the sugarcane bagasse (despite using a sifter to separate the particles of a specific mesh range). In this case, bigger particle sizes would lead to higher surface areas.[87]

It is also possible that the sugarcane bagasse weighed for each sample preparation had different pith/fiber ratios in the composition. It would affect the surface area of the samples because higher surface areas are achieved in samples containing high cellulosic contents.[88,89]

Statistical analysis was performed to establish the effect of each experimental parameter on adsorption-related parameters, as well as assess how their correlation affected the surface of the AC X-Y-Z samples. SI section portrays the results and the respective discussion.

### Adsorption and desorption of urea

This work aimed at the application of the activated carbon as a fertilizer-releasing system. Hence, its adsorption and desorption assays were performed using urea complexed with *p*-DMAB. This reaction converts urea into a chromophore compound that absorbs within the ultraviolet/visible range.[42] Figure 5 depicts the obtained results regarding the adsorptive capacity and desorption of complexed urea.

AC 400-11-900 presented a mean adsorptive capacity of (758.7 ± 263.8) mg $g^{-1}$. This high standard deviation (SD) comes from the experimental conditions. Since the aliquots were analyzed as collected (without any previous treatment like centrifugation), some solid particles possibly remained in the optical path, scattering the light and increasing the SD value. Despite the experimental limitation, it is still safe to say that the AC presented a high adsorptive capacity. The adsorption profile suggests that the AC has fast adsorption, too, reaching the equilibrium within 1.5 h. The presence of negatively charged oxygen atoms and oxygen-containing groups in this sample might justify this quick adsorption. These atoms can strongly interact with the $NH_2$ groups from the complexed urea by ion-dipole and dipole-dipole interactions (mostly hydrogen bonds).

The adsorptive capacity of AC 400-11-900 was considerably higher than the one reported by Khalil *et al.*[90] The authors added $ZnCl_2$ to SCB, and activated it at three different temperatures (400, 500, or 600 °C). Even though the AC activated at 600 °C presented a surface area of 1925.0 $m^2$ $g^{-1}$, its adsorptive capacity reached the maximum after adsorbing ca. 80.0 mg $g^{-1}$ of phenol. Besides, their AC reached the equilibrium after more than 4 h.

The adsorptive capacity observed in the present work was also higher than the one observed by Soudani *et al.*[91] Their activated carbons, produced from oak fruit shells, managed to adsorb 41.97 mg $g^{-1}$ of $Cu^{2+}$.

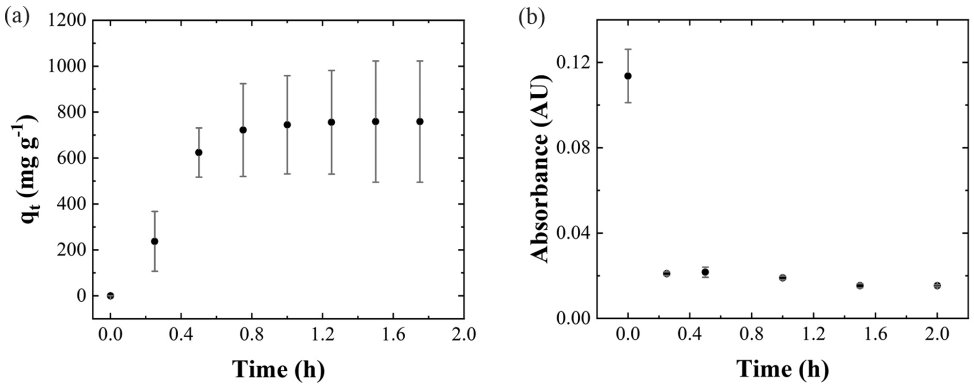


**Figure 5.** Curves of (a) adsorptive capacity ($q_t$; mg $g^{-1}$) and (b) desorption of complexed urea by sample AC 400-11-900.

Regarding the desorption assay, Figure 5b suggests that, not only did the AC maintain the complexed urea adsorbed onto its surface, but it also adsorbed the complexed urea molecules that remained in the solution after the removal of the solution used for the adsorption assay. It suggests the formation of strong physical bonds between AC and urea, stronger than the ones formed between urea and water, agreeing with the XPS results.

Assuming that this behavior would be faithfully reproducible under *in vivo* conditions, the AC would (*i*) effectively retain urea molecules adsorbed to it, releasing them as soil bacteria degrade the AC, and (*ii*) it could re-adsorb eventual urea molecules released to the soil that were not absorbed by the plant nor converted into volatile compounds. This strong interaction between the AC and urea would also prevent burst releases, ensuring a longer availability of urea to the plants. Moreover, the high adsorptive capacity suggest that smaller amounts of AC would be necessary to ensure the availability of urea in the required amounts. Once all the urea molecules release from the AC and that all the degradable compounds have been degraded, fulfilling its purpose of a fertilizer-releaser system, AC would still benefit the soil. However, *in vivo* assays are still required to evaluate the performance of AC as a fertilizer releasing system and to determine its suitability for such application. These analyses are prospects of this work.

## Conclusions

The present work reported the production of activated carbons from sugarcane bagasse using a solid-state reaction. The effect of the pyrolysis and activation temperature and the base concentration on the lattice parameters, surface area, area, and volume of micropores was assessed using the design of the experiments. The results indicated significant statistical differences at 95% for the combination of pyrolysis and activation temperatures regarding the crystallinity of peak $X_{c,2}$. The high temperatures employed in the pyrolysis and activation step decreased the percentage of crystallinity of the peak referent to plane 100 ($X_{c,2}$), but it increased the surface area, area, and volume of micropores in the ACs. The activation temperature also led to significant statistical differences in the crystallite diameter (La). Higher activation temperatures decreased this parameter by 2.8.

Zeta potential measures indicated that the samples activated at 600 °C were negatively charged throughout the entire pH range (from pH 3 to pH 9), while the ones activated at 900 °C displayed some positive charges at pHs < 4.0. An excess of functional groups in the side groups of the graphitic layers justifies this behavior. The surface area of the ACs reached 1401 $m^2$ $g^{-1}$ for the sample prepared with a pyrolysis temperature of 400 °C, a concentration of KOH equivalent to 11 mol $L^{-1}$, and an activation temperature of 900 °C (AC 400-11-900). This sample also portrayed type-II adsorption isotherm with hysteresis loops cut-off at $P/P_0$ ca. 0.5.

The sample with the highest surface area (AC 400-11-900) had an adsorptive capacity of (758.7 ± 263.8) mg $g^{-1}$, but it did not desorb the urea molecules when placed in the release medium. Intriguingly, the particles adsorbed even more urea molecules. That is particularly appealing for agricultural purposes because, if used as a fertilizer-releasing device, the AC would be able to re-adsorb urea molecules non-absorbed by the plant, sustaining nutrient availability for longer periods. Despite the *in vivo* evaluation of the efficiency of these ACs as fertilizer-releasing systems still being a prospect of this work, the *in vitro* results suggest that the material is very likely to contribute to soil fertilization and to prevent nutrient loss.

## Supplementary Information

Supplementary data are available free of charge at http://jbcs.sbq.org.br as a PDF file.

## Acknowledgments

The authors acknowledge the financial support provided by Coordenação de Aperfeiçoamento de Nível Superior (CAPES), Conselho Nacional de Desenvolvimento Científico Tecnológico (CNPq), and Instituto Nacional de Ciência e Tecnologia em Materiais Complexos Funcionais (INOMAT). The authors also acknowledge Financiadora de Estudos e Projetos (FINEP), Complexo de Centrais de Apoio à Pesquisa-UEM (Central de Microscopia (CMI)) for granting access to the microscopes used to characterize the samples.

### Author Contributions

Michelly Cristina G. Pellá was responsible for conceptualization, formal analysis, investigation, data curation, writing (original draft, review and editing), visualization; Andressa Renatta Simão for formal analysis, investigation, writing review and editing; Antônia Millena O. Lima for formal analysis, investigation, writing review and editing; Marcos Roberto Mauricio for investigation, writing review and editing; Guilherme M. Pereira for formal analysis, investigation; Rafael da Silva for conceptualization; Adley F. Rubira for conceptualization, investigation, writing (original draft, review and editing), visualization, supervision.

## References

1. Stahel, W. R.; *Nature* **2016**, *531*, 435. [Crossref]
2. Mu, X.; Li, Y.; Liu, X.; Ma, C.; Jiang, H.; Zhu, J.; Chen, X.; Tang, T.; Mijowska, E.; *Nanomaterials* **2020**, *10*, 1097. [Crossref]
3. Ao, W.; Fu, J.; Mao, X.; Kang, Q.; Ran, C.; Liu, Y.; Zhang, H.; Gao, Z.; Li, J.; Liu, G.; Dai, J.; *Renewable Sustainable Energy Rev.* **2018**, *92*, 958. [Crossref]
4. Hu, J.; Song, Y.; Liu, J.; Evrendilek, F.; Zhang, G.; Ren, M.; Xie, W.; Sun, S.; *Fuel* **2022**, *318*, 123603. [Crossref]
5. Saleem, J.; Shahid, U. Bin; Hijab, M.; Mackey, H.; McKay, G.; *Biomass Convers. Biorefin.* **2019**, *9*, 775. [Crossref]
6. Ghosh, S.; Santhosh, R.; Jeniffer, S.; Raghavan, V.; Jacob, G.; Nanaji, K.; Kollu, P.; Jeong, S. K.; Grace, A. N.; *Sci. Rep.* **2019**, *9*, 16315. [Crossref]
7. Mi, J.; Wang, X.-R.; Fan, R.-J.; Qu, W.-H.; Li, W.-C.; *Energy Fuels* **2012**, *26*, 5321. [Crossref]
8. Xiao, Z.; Chen, W.; Liu, K.; Cui, P.; Zhang, D.; *Int. J. Electrochem. Sci.* **2018**, *13*, 5370. [Crossref]
9. Subramani, K.; Sudhan, N.; Karnan, M.; Sathish, M.; *ChemistrySelect* **2017**, *2*, 11384. [Crossref]
10. Beyan, S. M.; Prabhu, S. V.; Sissay, T. T.; Getahun, A. A.; *Bioresour. Technol. Rep.* **2021**, *14*, 100664. [Crossref]
11. Heidarinejad, Z.; Dehghani, M. H.; Heidari, M.; Javedan, G.; Ali, I.; Sillanpää, M.; *Environ. Chem. Lett.* **2020**, *18*, 393. [Crossref]
12. Marsh, H.; Reinoso, F. R.; *Activated Carbon*, 1st ed.; Elsevier: London, UK, 2006.
13. Wong, S.; Ngadi, N.; Inuwa, I. M.; Hassan, O.; *J. Cleaner Prod.* **2018**, *175*, 361. [Crossref]
14. Zubrik, A.; Matik, M.; Hredzák, S.; Lovás, M.; Danková, Z.; Kováčová, M.; Briančin, J.; *J. Cleaner Prod.* **2017**, *143*, 643. [Crossref]
15. Bedia, J.; Peñas-Garzón, M.; Gómez-Avilés, A.; Rodriguez, J. J.; Belver, C.; *C* **2020**, *6*, 21. [Crossref]
16. Abuelnoor, N.; AlHajaj, A.; Khaleel, M.; Vega, L. F.; Abu-Zahra, M. R. M.; *Chemosphere* **2021**, *282*, 131111. [Crossref]
17. Singh, G.; Lakhi, K. S.; Kim, I. Y.; Kim, S.; Srivastava, P.; Naidu, R.; Vinu, A.; *ACS Appl. Mater. Interfaces* **2017**, *9*, 29782. [Crossref]
18. Thakur, A. K.; Sathyamurthy, R.; Velraj, R.; Lynch, I.; Saidur, R.; Pandey, A. K.; Sharshir, S. W.; Ma, Z.; GaneshKumar, P.; Kabeel, A. E.; *Desalination* **2021**, *516*, 115217. [Crossref]
19. Baig, M. M.; Gul, I. H.; *Biomass Bioenergy* **2021**, *144*, 105909. [Crossref]
20. Mariana, M.; H.P.S., A. K.; Mistar, E. M.; Yahya, E. B.; Alfatah, T.; Danish, M.; Amayreh, M.; *J. Water Process Eng.* **2021**, *43*, 102221. [Crossref]
21. Nizam, N. U. M.; Hanafiah, M. M.; Mahmoudi, E.; Halim, A. A.; Mohammad, A. W.; *Sci. Rep.* **2021**, *11*, 8623. [Crossref]
22. Rashid, M.; Hussain, Q.; Khan, K. S.; Alwabel, M. I.; Hayat, R.; Akmal, M.; Ijaz, S. S.; Alvi, S.; Obaid-ur-Rehman; *J. Soil Sci. Plant Nutr.* **2021**, *21*, 1144. [Crossref]
23. Arslanoğlu, H.; Tümen, F.; *Process Saf. Environ. Prot.* **2021**, *147*, 1077. [Crossref]
24. Vejan, P.; Abdullah, R.; Ahmad, N.; Khadiran, T.; *Environ. Sci. Pollut. Res.* **2022**, *30*, 38738. [Crossref]
25. Chen, X.; Jeyaseelan, S.; Graham, N.; *Waste Manage.* **2002**, *22*, 755. [Crossref]
26. Tanaka, H.; *Thermochim. Acta* **1995**, *267*, 29. [Crossref]
27. Manikandan, A.; Subramanian, K. S.; *Indian J. Sci. Technol.* **2013**, *6*, 5579. [Link] accessed in January 2024
28. Uchimiya, M.; Lima, I. M.; Klasson, K. T.; Wartelle, L. H.; *Chemosphere* **2010**, *80*, 935. [Crossref]
29. Lehmann, J.; da Silva Jr., J. P.; Steiner, C.; Nehls, T.; Zech, W.; Glaser, B.; *Plant Soil* **2003**, *249*, 343. [Crossref]
30. Sanchez, P. A.; *Soil Sci.* **1977**, *124*, 187. [Link] accessed in January 2024
31. Fragal, E. H.; Cellet, T. S. P.; Fragal, V. H.; Companhoni, M. V. P.; Ueda-Nakamura, T.; Muniz, E. C.; Silva, R.; Rubira, A. F.; *Carbohydr. Polym.* **2016**, *152*, 734. [Crossref]
32. Zhang, F.; Ma, H.; Chen, J.; Li, G.-D.; Zhang, Y.; Chen, J.-S.; *Bioresour. Technol.* **2008**, *99*, 4803. [Crossref]
33. Saad, M. J.; Chia, C. H.; Zakaria, S.; Sajab, M. S.; Misran, S.; Abdul Rahman, M. H.; Chin, S. X.; *Sains Malays.* **2019**, *48*, 385. [Crossref]

34. Meng, J.; Li, S.; Niu, J.; *ACS Omega* **2019**, *4*, 20762. [Crossref]
35. Lu, L.; Sahajwalla, V.; Harris, D.; *Energy Fuels* **2000**, *14*, 869. [Crossref]
36. Biscoe, J.; Warren, B. E.; *J. Appl. Phys.* **1942**, *13*, 364. [Crossref]
37. Takagi, H.; Maruyama, K.; Yoshizawa, N.; Yamada, Y.; Sato, Y.; *Fuel* **2004**, *83*, 2427. [Crossref]
38. *CasaXPS Processing Software*, version 2.3.25; Casa Software Ltd., Teignmouth, UK, 2021.
39. Polovina, M.; Babić, B.; Kaluderović, B.; Dekanski, A.; *Carbon* **1997**, *35*, 1047. [Crossref]
40. Pellá, M. C. G.; Simão, A. R.; Valderrama, P.; Rubira, A. F.; *Anal. Methods* **2023**, *15*, 2016. [Crossref]
41. Pavia, D. L.; Lampman, G. M.; Kriz, G. S.; Vyvyan, J. A.; *Introduction to Spectroscopy*, 4th ed.; Cengage Learning: Boston, Massachusetts, USA, 2008.
42. Knorst, M. T.; Neubert, R.; Wohlrab, W.; *J. Pharm. Biomed. Anal.* **1997**, *15*, 1627. [Crossref]
43. *Statistica*, version 10; StatSoft, Tulsa, OK, USA, 2011.
44. *Minitab*, version 16; Minitab Inc., State College, PA, USA, 2021.
45. Bruice, P. Y.; *Organic Chemistry*, 8th ed.; Pearson: Upper Saddle River, USA, 2017.
46. Han, J.; Zhang, L.; Zhao, B.; Qin, L.; Wang, Y.; Xing, F.; *Ind. Crops Prod.* **2019**, *128*, 290. [Crossref]
47. Girgis, B. S.; Temerk, Y. M.; Gadelrab, M. M.; Abdullah, I. D.; *Carbon Lett.* **2007**, *8*, 95. [Crossref]
48. Du, F.; Zhang, M.; Li, X.; Li, J.; Jiang, X.; Li, Z.; Hua, Y.; Shao, G.; Jin, J.; Shao, Q.; Zhou, M.; Gong, A.; *Nanotechnology* **2014**, *25*, 315702. [Crossref]
49. Eslami, A.; Borghei, S. M.; Rashidi, A.; Takdastan, A.; *Sep. Sci. Technol.* **2018**, *53*, 2536. [Crossref]
50. Bedin, K. C.; Martins, A. C.; Cazetta, A. L.; Pezoti, O.; Almeida, V. C.; *Chem. Eng. J.* **2016**, *286*, 476. [Crossref]
51. Tee, E.; Tallo, I.; Kurig, H.; Thomberg, T.; Jänes, A.; Lust, E.; *Electrochim. Acta* **2015**, *161*, 364. [Crossref]
52. Dresselhaus, M. S.; Dresselhaus, G.; Hofmann, M.; *Vib. Spectrosc.* **2007**, *45*, 71. [Crossref]
53. Liu, Y.; Pan, C.; Wang, J.; *J. Mater. Sci.* **2004**, *39*, 1091. [Crossref]
54. Escribano, R.; Sloan, J. J.; Siddique, N.; Sze, N.; Dudev, T.; *Vib. Spectrosc.* **2001**, *26*, 179. [Crossref]
55. Kawakami, M.; Kanba, H.; Sato, K.; Takenaka, T.; Gupta, S.; Chandratilleke, R.; Sahajwalla, V.; *ISIJ Int.* **2006**, *46*, 1165. [Link] accessed in January 2024
56. Amaral Jr., M. A.; Matsushima, J. T.; Rezende, M. C.; Gonçalves, E. S.; Marcuzzo, J. S.; Baldan, M. R.; *J. Aerosp. Technol. Manage.* **2017**, *9*, 423. [Crossref]
57. Shimodaira, N.; Masui, A.; *J. Appl. Phys.* **2002**, *92*, 902. [Crossref]
58. Endo, M.; Nishimura, K.; Kim, Y. A.; Hakamada, K.; Matushita, T.; Dresselhaus, M. S.; Dresselhaus, G.; *J. Mater. Res.* **1999**, *14*, 4474. [Crossref]
59. Heise, H. M.; Kuckuk, R.; Ojha, A. K.; Srivastava, A.; Srivastava, V.; Asthana, B. P.; *J. Raman Spectrosc.* **2009**, *40*, 344. [Crossref]
60. Zhou, J.-H.; Sui, Z.-J.; Zhu, J.; Li, P.; Chen, D.; Dai, Y.-C.; Yuan, W.-K.; *Carbon* **2007**, *45*, 785. [Crossref]
61. Cook, R.; Crathorne, E. A.; Monhemius, A. J.; Perry, D. L.; *Hydrometallurgy* **1989**, *22*, 171. [Crossref]
62. Terzyk, A. P.; *Colloids Surf., A* **2001**, *177*, 23. [Crossref]
63. Driemeier, C.; Oliveira, M. M.; Mendes, F. M.; Gómez, E. O.; *Powder Technol.* **2011**, *214*, 111. [Crossref]
64. Abo El Naga, A. O.; El Saied, M.; Shaban, S. A.; El Kady, F. Y.; *J. Mol. Liq.* **2019**, *285*, 9. [Crossref]
65. Guo, Y.; Tan, C.; Sun, J.; Li, W.; Zhang, J.; Zhao, C.; *Chem. Eng. J.* **2020**, *381*, 122736. [Crossref]
66. Bhattacharjee, S.; *J. Control. Release* **2016**, *235*, 337. [Crossref]
67. Amoo, T. E.; Amoo, K. O.; Adeeyo, O. A.; Ogidi, C. O.; *Int. J. Chem. Eng.* **2022**, *2022*, ID 6928568. [Crossref]
68. Tang, C.; Shu, Y.; Zhang, R.; Li, X.; Song, J.; Li, B.; Zhang, Y.; Ou, D.; *RSC Adv.* **2017**, *7*, 16092. [Crossref]
69. Gonçalves, S. P. C.; Strauss, M.; Delite, F. S.; Clemente, Z.; Castro, V. L.; Martinez, D. S. T.; *Sci. Total Environ.* **2016**, *565*, 833. [Crossref]
70. Atkins, P. W.; De Paula, J.; *Atkins' Physical Chemistry*, 10th ed.; OUP Oxford: Oxford, UK, 2020.
71. Fagerlund, G.; *Mater. Constr.* **1973**, *6*, 239. [Crossref]
72. Sing, K.; *Colloids Surfaces, A* **2001**, *187-188*, 3. [Crossref]
73. Salvador, F.; Sánchez-Jiménez, C.; Sánchez-Montero, M. J.; Salvador, A. In *Studies in Surface Science and Catalysis*, vol. 144; Rodriguez-Reinoso, F.; McEnaney, B.; Rouquerol, J.; Unger, K., eds.; Elsevier, 2002, p. 379-386. [Crossref]
74. Muttakin, M.; Mitra, S.; Thu, K.; Ito, K.; Saha, B. B.; *Int. J. Heat Mass Transfer* **2018**, *122*, 795. [Crossref]
75. Khalfaoui, M.; Knani, S.; Hachicha, M. A.; Lamine, A. B.; *J. Colloid Interface Sci.* **2003**, *263*, 350. [Crossref]
76. Brunauer, S.; Emmett, P. H.; Teller, E.; *J. Am. Chem. Soc.* **1938**, *60*, 309. [Crossref]
77. Sing, K. S. W.; Williams, R. T.; *Adsorpt. Sci. Technol.* **2004**, *22*, 773. [Crossref]
78. Rengasamy, R. S. In *Thermal and Moisture Transport in Fibrous Materials*; Elsevier: Delhi, India, 2006, ch. 5, p. 156-187.
79. Yurdakal, S.; Garlisi, C.; Özcan, L.; Bellardita, M.; Palmisano, G. In *Heterogeneous Photocatalysis*, 1st ed.; Elsevier: London, UK, 2019, ch. 4.
80. Everett, D. H. In *Marcel Decker: New York*, 1st ed.; Marcel Decker: New York: New York, USA, 1967.
81. Gregg, S. J.; Sing, K. S. W.; Salzberg, H. W.; *J. Electrochem. Soc.* **1967**, *114*, 279C. [Crossref]
82. Esteban, N.; Ferrer, M. L.; Ania, C. O.; de la Campa, J. G.; Lozano, Á. E.; Álvarez, C.; Miguel, J. A.; *ACS Appl. Mater. Interfaces* **2020**, *12*, 56974. [Crossref]

83. Demiral, H.; Demiral, İ.; *Surf. Interface Anal.* **2008**, *40*, 612. [Crossref]
84. Burgess, C. G. V.; Everett, D. H.; Nuttall, S.; *Pure Appl. Chem.* **1989**, *61*, 1845. [Crossref]
85. Tanev, P. T.; Vlaev, L. T.; *J. Colloid Interface Sci.* **1993**, *160*, 110. [Crossref]
86. Silvestre-Albero, A. M.; Juárez-Galán, J. M.; Silvestre-Albero, J.; Rodríguez-Reinoso, F.; *J. Phys. Chem. C* **2012**, *116*, 16652. [Crossref]
87. Caturla, F.; Molina-Sabio, M.; Rodríguez-Reinoso, F.; *Carbon* **1991**, *29*, 999. [Crossref]
88. Pandey, A.; Soccol, C. R.; Nigam, P.; Soccol, V. T.; *Bioresour. Technol.* **2000**, *74*, 69. [Crossref]
89. Dwiyaniti, M.; Elang Barruna, A.; Muhamad Naufal, R.; Subiyanto, I.; Setiabudy, R.; Hudaya, C.; *IOP Conf. Ser.: Mater. Sci. Eng.* **2020**, *909*, 012018. [Crossref]
90. Khalil, K. M. S.; Khairy, M.; Allam, O. A. S.; Khalil, M. K.; *Int. J. Environ. Sci. Technol.* **2022**, *19*, 3103. [Crossref]
91. Soudani, A.; Youcef, L.; Bulgariu, L.; Youcef, S.; Toumi, K.; Soudani, N.; *Chem. Eng. Res. Des.* **2022**, *188*, 972. [Crossref]

*Submitted: November 10, 2023*
*Published online: February 1, 2024*